

Thermal and thermoelectric properties of an antiferromagnetic topological insulator

MnBi_2Te_4

H. Zhang,¹ C.Q. Xu,¹ S.H. Lee,^{2,3} Z.Q. Mao,^{2,3} and X. Ke¹

¹ Department of Physics and Astronomy, Michigan State University, East Lansing, Michigan 48824, USA

² Department of Physics, Pennsylvania State University, University Park, Pennsylvania 16802, USA

³ 2D Crystal Consortium, Materials Research Institute, Pennsylvania State University, University Park, Pennsylvania 16802, USA

The discovery of an intrinsic antiferromagnetic topological insulator (AFM-TI) in MnBi_2Te_4 has attracted intense attention, most of which lies on its electrical properties. In this paper, we report electronic, thermal, and thermoelectric transport studies of this newly found AFM-TI. The temperature and magnetic field dependence of its resistivity, thermal conductivity, and Seebeck coefficient indicate strong coupling between charge, lattice, and spin degrees of freedom in this system. Furthermore, MnBi_2Te_4 exhibits a large anomalous Nernst signal, which is associated with non-zero Berry curvature of the field-induced canted antiferromagnetic state.

Intrinsic magnetic topological materials have been intensely sought after by researchers in materials science and condense matter physics communities in the past few years¹⁻¹⁰. In particular, the integration of magnetism and non-trivial band topology in magnetic topological insulators (MTIs) provides an ideal ground for identifying exotic states and quasiparticles, such as quantum anomalous Hall insulator, axion insulator and non-Abelian Majorana fermions¹¹⁻¹³. Three routes to search for new MTIs have been actively explored, including doping topological insulators (TIs) with magnetic elements¹⁴, building heterostructures by stacking TIs and magnetic layers together¹⁵, and synthesizing single-phase materials which can host magnetism and topological bands¹⁰. The recent discovery of the characteristics of an intrinsic MTI in MnBi_2Te_4 (MBT)⁸ marks a major advancement in the latter route, which further attracts avid efforts in exploring all aspects of this newly found MTI^{11,13,16-21} and its derivatives²²⁻²⁸.

In MBT the magnetic order is associated with the Manganese atoms, the non-trivial band topology arises from the p_z bands of Bismuth and Tellurium⁸. It undergoes a paramagnetic-to-antiferromagnetic order at $T_N = 25$ K with an A-type spin structure where spins are ferromagnetically aligned within the ab -plane but coupled antiferromagnetically along the c -axis^{16,21}. And the system has a magnetic easy-axis along the c -direction²¹. The antiferromagnetic ground state is predicted to gap out both bulk and surface states and create an axion insulator state, while Weyl semimetal is proposed to emerge in the ferromagnetic phase^{7,17}. Indeed, the observation of robust axion insulator state has been reported recently¹¹, and the field-induced topological phase transition has been inferred from recent electronic transport studies^{29,30}. These theoretical predictions and experimental studies demonstrate that new quantum states can be achieved in a system wherein intrinsic magnetism and non-trivial band topology couples strongly.

Thus far, most studies of MBT are mainly focused on the interplay between magnetism and band topology, while the lattice degree of freedom and its potential coupling to the spin and charge degrees of freedom remain largely unexplored. In recent inelastic neutron scattering experiments, intrinsic linewidth broadening of the spin wave spectrum has been observed, which was attributed to coupling of magnons to either phonons or electrons²⁰. More recently, terahertz (THZ) experiment demonstrated coherent magneto-phononic coupling in MnBi_2Te_4 , which enables sub-picosecond control of magnetism with ultrafast laser³¹. These studies imply the strong coupling between spin and lattice degree of freedom in MBT. While recently H. H. Wang et al reported the temperature dependence of zero-field thermal conductivity and Seebeck coefficient in $\text{Mn}(\text{Bi}_{1-x}\text{Sb}_x)_2\text{Te}_4$ ³², they focused on the hole-doping effect induced by Sb substitution. In this paper, we report thermal and thermoelectric properties of MBT. We show that both thermal conductivity and Seebeck coefficient strongly depend on the applied magnetic field, indicative of the strong coupling between charge, lattice, and spin degrees of freedom in MBT. In addition, we observe a clear anomalous Nernst effect (ANE) feature, which is presumably ascribed to the non-zero Berry curvature in the field-induced canted antiferromagnetic phase.

MBT single crystals were grown using flux method²¹. Magnetic susceptibility measurements were carried out using a Superconducting Quantum Interference Device (SQUID) magnetometer, and the electronic and thermal and thermoelectric transport measurements were conducted using a Physical Property Measurement System (PPMS). Thermal and thermoelectric transport measurements were performed using a homemade sample puck designed to be compatible with the PPMS cryostat. The sample was attached to a piece of oxygen-free high conductivity copper used as the heat sink using silver epoxy, and a heater ($\sim 1\text{ k}\Omega$ resistor) was attached to the other end of the sample. The heat current J_Q was applied in the ab plane and the

magnetic field was applied along the c -axis. We used three Cernox (Lakeshore Cryotronics) sensors for the temperature measurements, and the thermoelectric voltage was measured using K2182A Nanovoltmeters. The Nernst and Seebeck coefficients were obtained by antisymmetrizing and symmetrizing the thermoelectric voltages measured in the presence of positive field and negative field, respectively.

Figure 1(a) shows the temperature dependence of zero-field cooled magnetic susceptibility measured with 1 T field applied along the crystalline c -axis (χ_c) during the warming process. A sharp drop in χ_c at the Neel temperature ($T_N = 25$ K) is clearly seen, characteristic of the onset of antiferromagnetic transition. The isothermal magnetization curves $M(H)$ measured at various temperature from 2 K to 30 K are presented in Fig. 1(b). Below T_N , field induced metamagnetic transition occurs at the critical field (H_{c1}) which depends on the temperature. Previous transport and neutron scattering measurements showed that a canted antiferromagnetic phase emerges above H_{c1} ²¹. Another critical magnetic field H_{c2} with larger magnitude is expected, above which MBT becomes fully polarized²¹. The nice agreement of magnetic susceptibility presented in Fig. 1 with the literature²¹ affirms the good sample quality of our single crystals.

We now discuss the temperature dependence of electronic, thermal, and thermoelectric properties of MBT. In Fig. 2(a) we show the Seebeck coefficient (S_{xx}) and resistivity (ρ_{xx}) of MBT measured at a field of 0 T and 9 T applied along the c -axis. At zero field, a kink-like transition around the Neel temperature is observed in both S_{xx} and ρ_{xx} . A previous transport study has found that the spin fluctuation-driven scattering has a prominent effect in MBT, even well above T_N ²¹. Upon approaching T_N , spin fluctuations are expected to be stronger, leading to stronger scattering and thus a shorter mean-free-path of electrons and an increase in ρ_{xx} . As the long-range magnetic order develops below T_N , in which spins within the ab plane are ferromagnetically aligned, spin

fluctuations and the electron-spin scattering are suppressed, resulting in a kink in ρ_{xx} at T_N followed by a continuous decrease upon decreasing the temperature. For S_{xx} , its negative sign over the whole measured temperature range suggests electrons as the dominant charge carriers, which is consistent with the Hall effect transport studies²¹. The negative sign of S_{xx} was also previously observed, although only S_{xx} above 15 K was reported³² and its magnitude is different from the values shown in Fig. 1(a), the latter of which is presumably associated with the quality of samples grown by different groups. As the temperature decreases, the entropy per electron decreases³³, leading to a decrease in S_{xx} ; on the other hand, as will be discussed later, below T_N the magnon-electron drag effect due to the coherent momentum conserving magnon-electron scattering gives rise to an increase in S_{xx} . As a result, the net S_{xx} develops a broad bump around 14 K. At 9 T, MBT becomes a fully polarized ferromagnet, which increases the magnon lifetime and thus enhances the magnon-electron drag effect. Overall, these features of S_{xx} and ρ_{xx} indicate that the spin and charge degrees of freedom are intimately coupled in MBT.

Figure 2(b) shows the thermal conductivity (κ_{xx}) measured at 0 T and 9 T magnetic field ($H \parallel c$). At zero field, we observe a large increase of κ_{xx} upon the onset of antiferromagnetic ordering at T_N . The total thermal conductivity in MBT has contributions from electrons, phonons, and magnons (i. e., $\kappa_{xx} = \kappa^e + \kappa^{ph} + \kappa^{mag}$). We first estimate the thermal conductivity of electrons (κ^e) using Wiedemann-Franz law ($\kappa^e = \sigma LT, L = 2.44 * 10^{-8} V^2/K^2$). The maximum electron contribution below 25 K is $0.05 W/m K$, much smaller than the increase of thermal conductivity κ_{xx} observed below T_N . Therefore, the main heat carriers in MBT are phonons and / or magnons. Magnons can contribute to the thermal conduction via two ways. One is that magnons serve as heat carriers, which would lead to an enhanced κ_{xx} below T_N ; the other is that magnons scatter phonons, giving rise to a reduction of the phonon contribution to κ_{xx} . Thus, the increase of

κ_{xx} below T_N indicates the dominance of magnons as heat carriers. In addition, well below T_N κ_{xx} at 9 T is smaller than the value measured at zero field, which can be ascribed to the suppression of magnon population in the presence of magnetic field, suggesting that magnons contribute to the enhanced κ_{xx} below T_N . On the other hand, the increase of κ_{xx} near T_N in the presence of 9 T is a sign of the dominant phonon scattering by magnons. As will be discussed later, the magnetic field dependence of κ_{xx} below T_N shows non-monotonic behavior, suggesting that in MBT the spin and lattice degrees of freedom are also intertwined.

The prominent effects of magnetic field on the temperature dependence of $\rho_{xx}, \kappa_{xx}, S_{xx}$ indicate that the spin, lattice, and charge degrees of freedom are strongly coupled in MBT. To better understand this coupling, we further investigate the field dependence of these three quantities. Note that a similar field dependence of ρ_{xx} has been reported previously²¹. In Fig. 3(a), we plot the field dependence of $\Delta\kappa_{xx}/\kappa_{xx}(0)$ with $\Delta\kappa_{xx} = \kappa_{xx}(\mu_0 H) - \kappa_{xx}(0)$ measured at some selected temperatures. Each curve is vertically shifted for clarity. Above T_N , κ_{xx} increases monotonically with magnetic field due to the suppression of spin-fluctuation driven phonon scattering. In contrast, below T_N , κ_{xx} exhibits a non-monotonic field dependence. At $T = 21.5$ K, κ_{xx} first decreases until the magnetic field reaches the first critical field H_{c1} and then continues to increase with the magnetic field. As the temperature decreases, a second critical field H_{c2} is observed prior to the continuous increase of κ_{xx} with the magnetic field. Both H_{c1} and H_{c2} increase upon decreasing the temperature. Such a field dependence of κ_{xx} below T_N is mainly associated with the spin state of MBT in the presence of field. Previous neutron diffraction measurements show that MBT displays an A-type antiferromagnetic structure for $H < H_{c1}$ and then a canted-antiferromagnetic (CAF) spin structure in the region of $H_{c1} < H < H_{c2}$ followed by a field-induced fully-polarized spin state above H_{c2} ²¹. Therefore, for $H < H_{c1}$ the application

of magnetic field suppresses the magnon population, thus reducing the magnon contribution κ^{mag} to the total κ_{xx} . For $H_{c1} < H < H_{c2}$, while the magnetic field continues to suppress the magnon population and reduces its contribution to κ_{xx} , the phonon scattering due to the magnon is reduced as well, which tends to enhance the phonon contribution to κ_{xx} . As a result of these competing effects, κ_{xx} decreases slightly in this intermediate field region. Finally, in the fully polarized state at $H > H_{c2}$ the magnon population further decreases as the magnon gap increases with the magnetic field, which leads to the dominant phonon contribution due to the suppression of magnon-phonon interaction over the magnon contribution, thus giving rise to an enhancement in the total κ_{xx} .

Figure 3(b) shows the change of Seebeck coefficient $\Delta S_{xx}/S_{xx}(0)$ with $\Delta S_{xx} = S_{xx}(\mu_0 H) - S_{xx}(0)$ as a function of magnetic field. Above T_N , S_{xx} increases with magnetic field; below T_N , S_{xx} first decreases with the applied field at $H < H_{c1}$ and then sharply increase at H_{c1} . At $H_{c1} < H < H_{c2}$, S_{xx} shows a bowl shape as a function of magnetic field; above H_{c2} , S_{xx} continues to increase with field again. Can the variation in S_{xx} in the presence of magnetic field arise from the magnetic field effect of the electron diffusion contribution? In metallic systems, one may anticipate that diffusion thermoelectric effect follows Mott relation, $S_{xx} = -\frac{\pi^2 k_B^2 T}{3e\sigma_{xx}} \frac{d\sigma_{xx}}{d\zeta} \Big|_{\mu}$ (μ is the Fermi energy). Assuming that the energy derivative of conductivity at Fermi energy $\frac{d\sigma_{xx}}{d\zeta} \Big|_{\mu}$ is constant, one would expect S_{xx} to increase with the increase of resistivity $\rho_{xx} (= 1/\sigma_{xx})$, which is opposite to the trends of field dependence of S_{xx} and ρ_{xx} shown in Fig. 3(b,c). Thus, one potential scenario is that the $\frac{d\sigma_{xx}}{d\zeta} \Big|_{\mu}$ term is field-dependent, having an opposite trend to and dominating over the field dependence of ρ such that S_{xx} increases while ρ_{xx} decreases with field. Alternatively, the magnetic field dependence of $\Delta S_{xx}/S_{xx}(0)$ shown in Fig. 3(b) may

be associated with the magnon-electron drag effect. In the presence of a temperature gradient, magnons may scatter electrons, causing a drag in electron velocity and enhancing S_{xx} . The initial decrease of S_{xx} at $H < H_{c1}$ is likely due to the reduction of magnon population and the resulting suppression of the magnon-electron drag process. Across H_{c1} , the magnetic structure changes from an A-type antiferromagnet to a canted antiferromagnet²¹. As a result, the magnon relaxation lifetime τ_m and the lifetime of electron scattered by magnon (τ_{em}) are altered. In the leading order approximation, the magnon-electron drag thermoelectric effect is proportional to τ_m/τ_{em} ³⁴. Thus, a potential dominant increase of τ_m compared to that of τ_{em} in the canted antiferromagnet state can lead to an enhanced S_{xx} . At H_{c2} MBT becomes a fully polarized ferromagnet²¹, which can reduce the magnon scattering at the magnetic domain walls and consequently further increases τ_m and magnon-electron drag effect in S_{xx} . Another possible mechanism that might account for the field dependence of S_{xx} is associated with the field-induced electronic structure change in MBT. That is, MBT undergoes topological phase transition from antiferromagnetic topological insulator to Weyl semimetal in the ferromagnetic state^{7,17,30}. Further theoretical investigation is desirable to pin down the underlying physics of the observed $S_{xx}(H)$ behavior.

Finally, we discuss the transverse thermoelectric transport, i.e., anomalous Nernst effect (ANE) in MBT. Recently, there has been increasing interest in the ANE effect in topological materials³⁵⁻³⁹. ANE is complementary to anomalous Hall effect (AHE) measurements in characterizing the Berry curvature distribution in the reciprocal space³⁸. Recent AHE studies suggested that a non-zero Berry curvature is created in the canted AFM state, leading to an intrinsic AHE²¹. In Fig. 4 we present the magnetic field dependence of Nernst coefficient ($-S_{xy}$) measured at various temperatures. The inset illustrates the schematic experimental setup and the sign convention here follows a previous ANE study on a Dirac semimetal Cd_3As_2 ³⁹. Overall, the Nernst

signal tracks well with the magnetization data [Fig. 1(b)] in behavior. Below T_N , the Nernst coefficient slowly increases with the magnetic field until H_{c1} at which a sudden increase in Nernst coefficient is observed, consistent with the emergence of non-zero Berry curvature in the momentum space in the canted antiferromagnetic phase suggested previously based on AHE measurements²¹. As the magnetic field is increased, MBT becomes fully polarized at H_{c2} ²¹ and turns into a Weyl semimetal^{7,17,29,30}. Nevertheless, recent electronic transport studies showed that the Weyl nodes in the polarized ferromagnetic state are not close to the Fermi energy in the pristine compound, in contrast to the lightly hole-doped $\text{Mn}(\text{Bi}_{1-x}\text{Sb}_x)_2\text{O}_4$ sample²⁹. As a result, the slight further enhancement in $|S_{xy}|$ above H_{c2} is mainly ascribable to the normal Nernst contribution instead of field-induced electronic structure change.

In summary, we have studied electronic, thermal and thermoelectric transport properties of MnBi_2Te_4 . We observe both temperature and magnetic field dependence of longitudinal resistivity, thermal conductivity, and Seebeck coefficient, indicating strong coupling among charge, lattice, and spin degrees of freedom in this system. Furthermore, the observation of anomalous Nernst effect implies the creation of Berry curvature in the momentum space in the field-induced canted antiferromagnetic state.

Acknowledgement

H.Z. and X.K. acknowledge the financial support by the U.S. Department of Energy, Office of Science, Office of Basic Energy Sciences, Materials Sciences and Engineering Division under DE-SC0019259. C.X. is partially supported by the Start-up funds at Michigan State University. The financial support for sample preparation was provided by the National Science Foundation through

the Penn State 2D Crystal Consortium-Materials Innovation Platform (2DCC-MIP) under NSF cooperative agreement DMR-1539916.

Figure 1

H. Zhang et al,

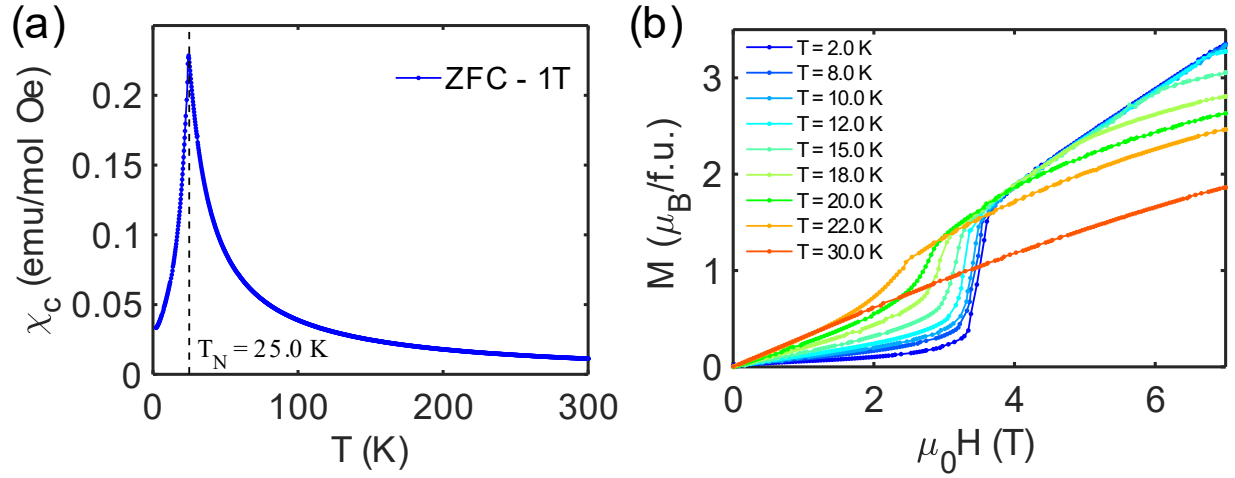


Figure 1. (a) Temperature dependence of magnetic susceptibility of MnBi_2Te_4 measured with a 1T magnetic field applied along the crystalline c -axis. The sample is cooled under zero-field conditions. (b) Isothermal magnetization measurement of MnBi_2Te_4 at various temperatures from 2 K to 30 K.

Figure 2

H. Zhang et al,

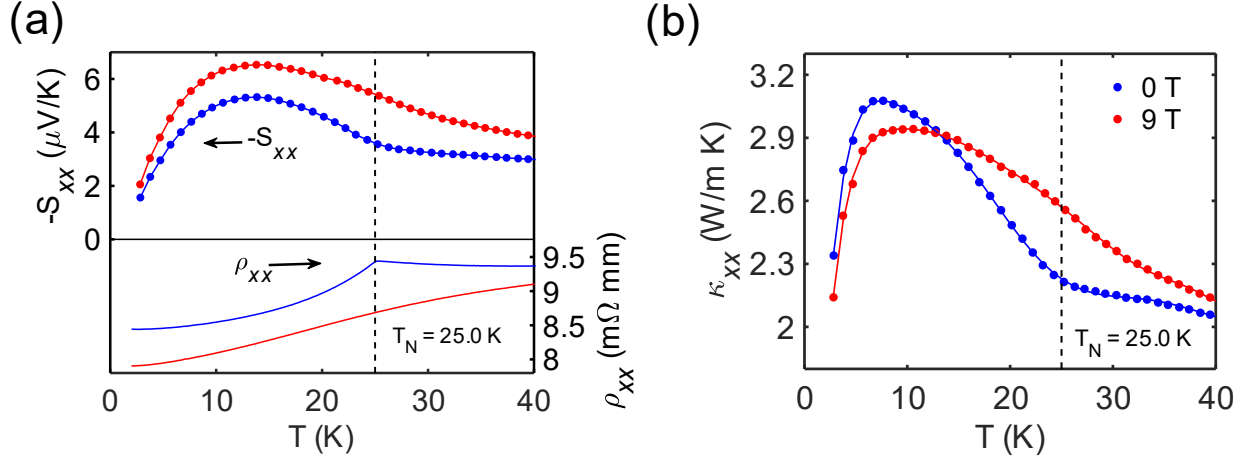


Figure 2. (a) Temperature dependence of longitudinal Seebeck coefficient S_{xx} (upper panel) and resistivity ρ_{xx} (lower panel) of MnBi₂Te₄ measured under an applied field of 0 T (in blue) and 9 T (in red, $H//c$). (b) Temperature dependence of longitudinal thermal conductivity κ_{xx} measured under an applied field of 0 T (in blue) and 9 T (in red, $H//c$).

Figure 3

H. Zhang et al,

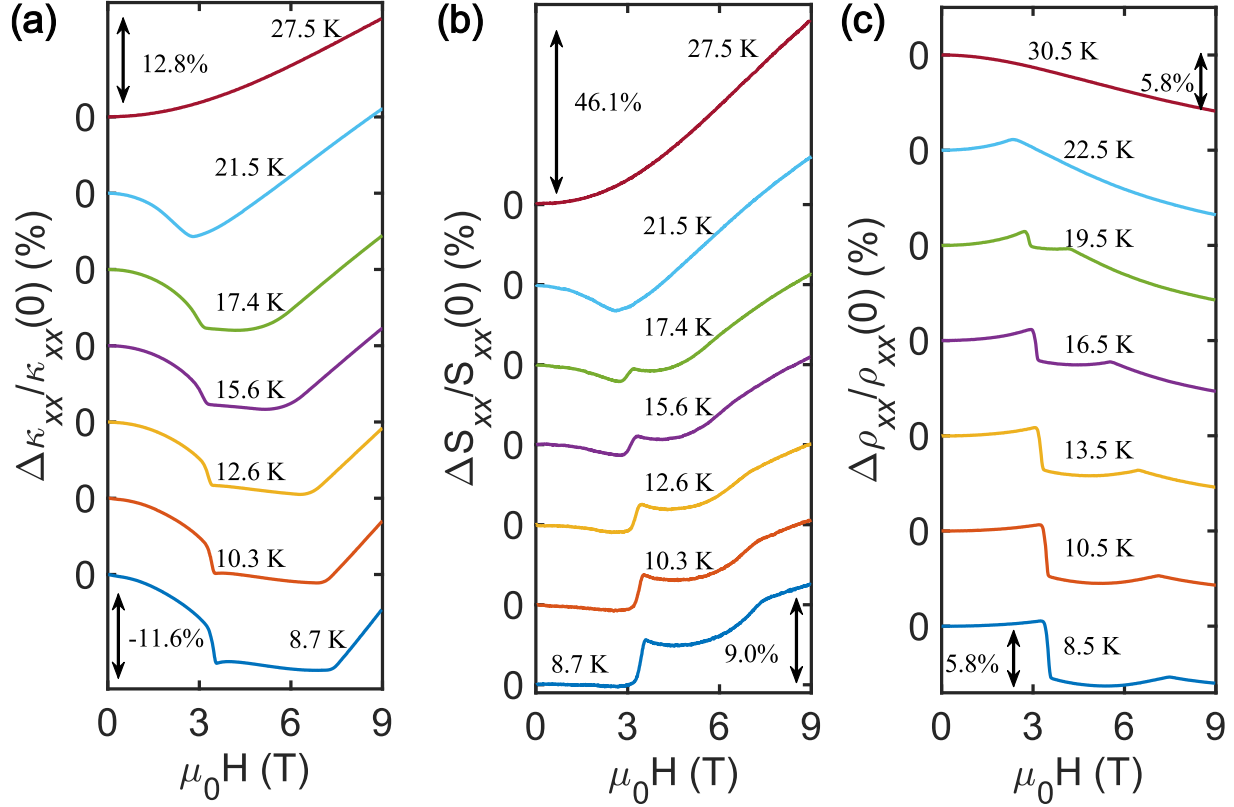


Figure 3. The magnetic field dependence of relative change in longitudinal (a) thermal conductivity κ_{xx} , (b) Seebeck coefficients S_{xx} , and (c) resistivity ρ_{xx} measured at various temperatures.

Figure 4

H. Zhang et al,

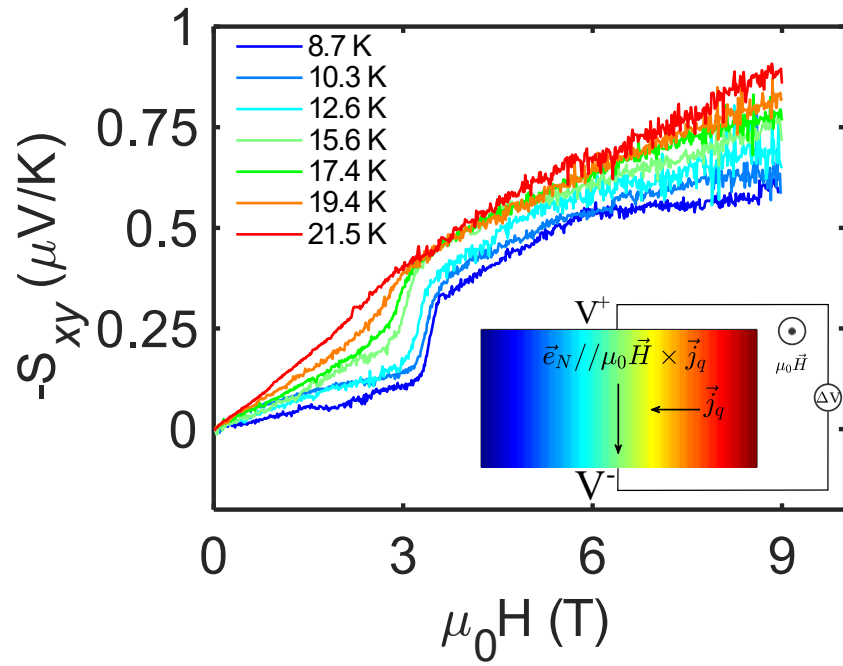


Figure 4. Magnetic field dependence of Nernst coefficients of MnBi_2Te_4 measured at various temperatures. The inset shows a schematic of the experimental set-up.

References

- 1 Nakatsuji, S., Kiyohara, N. & Higo, T. Large anomalous Hall effect in a non-collinear antiferromagnet at room temperature. *Nature* **527**, 212-215, doi:10.1038/nature15723 (2015).
- 2 Hirschberger, M. *et al.* The chiral anomaly and thermopower of Weyl fermions in the half-Heusler GdPtBi. *Nature Materials* **15**, 1161-1165, doi:10.1038/nmat4684 (2016).
- 3 Suzuki, T. *et al.* Large anomalous Hall effect in a half-Heusler antiferromagnet. *Nature Physics* **12**, 1119-1123, doi:10.1038/nphys3831 (2016).
- 4 Liu, E. *et al.* Giant anomalous Hall effect in a ferromagnetic kagome-lattice semimetal. *Nature Physics* **14**, 1125-1131, doi:10.1038/s41567-018-0234-5 (2018).
- 5 Sakai, A. *et al.* Giant anomalous Nernst effect and quantum-critical scaling in a ferromagnetic semimetal. *Nature Physics* **14**, 1119-1124, doi:10.1038/s41567-018-0225-6 (2018).
- 6 Ye, L. *et al.* Massive Dirac fermions in a ferromagnetic kagome metal. *Nature* **555**, 638-642, doi:10.1038/nature25987 (2018).
- 7 Li, J. *et al.* Intrinsic magnetic topological insulators in van der Waals layered MnBi₂Te₄-family materials. *Science Advances* **5**, eaaw5685, doi:10.1126/sciadv.aaw5685 (2019).
- 8 Otrokov, M. M. *et al.* Prediction and observation of an antiferromagnetic topological insulator. *Nature* **576**, 416-422, doi:10.1038/s41586-019-1840-9 (2019).
- 9 Tokura, Y., Yasuda, K. & Tsukazaki, A. Magnetic topological insulators. *Nature Reviews Physics* **1**, 126-143, doi:10.1038/s42254-018-0011-5 (2019).
- 10 Ning, W. & Mao, Z. Recent advancements in the study of intrinsic magnetic topological insulators and magnetic Weyl semimetals. *APL Materials* **8**, 090701, doi:10.1063/5.0015328 (2020).
- 11 Liu, C. *et al.* Robust axion insulator and Chern insulator phases in a two-dimensional antiferromagnetic topological insulator. *Nature Materials* **19**, 522-527, doi:10.1038/s41563-019-0573-3 (2020).
- 12 He, Q. L. *et al.* Chiral Majorana fermion modes in a quantum anomalous Hall insulator–superconductor structure. *Science* **357**, 294-299 (2017).
- 13 Deng, Y. *et al.* Quantum anomalous Hall effect in intrinsic magnetic topological insulator MnBi₂Te₄. *Science* **367**, 895-900 (2020).
- 14 Chang, C.-Z. *et al.* Experimental observation of the quantum anomalous Hall effect in a magnetic topological insulator. *Science* **340**, 167-170 (2013).
- 15 Qian, X., Liu, J., Fu, L. & Li, J. J. S. Quantum spin Hall effect in two-dimensional transition metal dichalcogenides. *Science* **346**, 1344-1347 (2014).
- 16 Yan, J. Q. *et al.* Crystal growth and magnetic structure of MnBi₂Te₄. *Physical Review Materials* **3**, 064202, doi:10.1103/PhysRevMaterials.3.064202 (2019).
- 17 Zhang, D. *et al.* Topological Axion States in the Magnetic Insulator MnBi₂Te₄ with the Quantized Magnetoelectric Effect. *Physical Review Letters* **122**, 206401, doi:10.1103/PhysRevLett.122.206401 (2019).
- 18 Hao, Y.-J. *et al.* Gapless Surface Dirac Cone in Antiferromagnetic Topological Insulator MnBi₂Te₄. *Physical Review X* **9**, 041038, doi:10.1103/PhysRevX.9.041038 (2019).
- 19 Chen, Y. J. *et al.* Topological Electronic Structure and Its Temperature Evolution in Antiferromagnetic Topological Insulator MnBi₂Te₄. *Physical Review X* **9**, 041040, doi:10.1103/PhysRevX.9.041040 (2019).
- 20 Li, B. *et al.* Competing Magnetic Interactions in the Antiferromagnetic Topological Insulator MnBi₂Te₄. *Physical Review Letters* **124**, 167204, doi:10.1103/PhysRevLett.124.167204 (2020).
- 21 Lee, S. H. *et al.* Spin scattering and noncollinear spin structure-induced intrinsic anomalous Hall effect in antiferromagnetic topological insulator MnBi₂Te₄. *Physical Review Research* **1**, 012011, doi:10.1103/PhysRevResearch.1.012011 (2019).

- 22 Ding, L. *et al.* Crystal and magnetic structures of magnetic topological insulators MnBi_2Te_4 and MnBi_4Te_7 . *Physical Review B* **101**, 020412, doi:10.1103/PhysRevB.101.020412 (2020).
- 23 Hu, Y. *et al.* Universal gapless Dirac cone and tunable topological states in $(\text{MnBi}_2\text{Te}_4)_m(\text{Bi}_2\text{Te}_3)_n$ heterostructures. *Physical Review B* **101**, 161113, doi:10.1103/PhysRevB.101.161113 (2020).
- 24 Vidal, R. C. *et al.* Orbital Complexity in Intrinsic Magnetic Topological Insulators MnBi_4Te_7 and $\text{MnBi}_6\text{Te}_{10}$. *Physical Review Letters* **126**, 176403, doi:10.1103/PhysRevLett.126.176403 (2021).
- 25 Vidal, R. C. *et al.* Topological Electronic Structure and Intrinsic Magnetization in MnBi_4Te_7 : A Bi_2Te_3 Derivative with a Periodic Mn Sublattice. *Physical Review X* **9**, 041065, doi:10.1103/PhysRevX.9.041065 (2019).
- 26 Hu, C. *et al.* A van der Waals antiferromagnetic topological insulator with weak interlayer magnetic coupling. *Nature Communications* **11**, 97, doi:10.1038/s41467-019-13814-x (2020).
- 27 Hu, C. *et al.* Realization of an intrinsic ferromagnetic topological state in $\text{MnBi}_8\text{Te}_{13}$. *Science Advances* **6**, eaba4275 (2020).
- 28 Tian, S. *et al.* Magnetic topological insulator $\text{MnBi}_6\text{Te}_{10}$ with a zero-field ferromagnetic state and gapped Dirac surface states. *Physical Review B* **102**, 035144, doi:10.1103/PhysRevB.102.035144 (2020).
- 29 Lee, S. H. *et al.* Evidence for a Magnetic-Field-Induced Ideal Type-II Weyl State in Antiferromagnetic Topological Insulator $\text{Mn}(\text{Bi}_{1-x}\text{Sb}_x)_2\text{Te}_4$. *Physical Review X* **11**, 031032, doi:10.1103/PhysRevX.11.031032 (2021).
- 30 Jiang, Q. *et al.* Quantum oscillations in the field-induced ferromagnetic state of $\text{MnBi}_{2-x}\text{Sb}_x\text{Te}_4$. *Physical Review B* **103**, 205111, doi:10.1103/PhysRevB.103.205111 (2021).
- 31 Padmanabhan, H. *et al.* Sub-picosecond coherent magnetophononic coupling in MnBi_2Te_4 . *Arxiv* (2021).
- 32 Wang, H. H. *et al.* Possible bipolar effect inducing anomalous transport behavior in the magnetic topological insulator $\text{Mn}(\text{Bi}_{1-x}\text{Sb}_x)_2\text{Te}_4$. *Physical Review B* **103**, 085126, doi:10.1103/PhysRevB.103.085126 (2021).
- 33 Behnia, K. & Aubin, H. Nernst effect in metals and superconductors: a review of concepts and experiments. *Reports on Progress in Physics* **79**, 046502, doi:10.1088/0034-4885/79/4/046502 (2016).
- 34 Polash, M. M. H., Mohaddes, F., Rasoulianboroujeni, M. & Vashaee, D. Magnon-drag thermopower in antiferromagnets versus ferromagnets. *Journal of Materials Chemistry C* **8**, 4049-4057, doi:10.1039/C9TC06330G (2020).
- 35 Ding, L. *et al.* Intrinsic Anomalous Nernst Effect Amplified by Disorder in a Half-Metallic Semimetal. *Physical Review X* **9**, 041061, doi:10.1103/PhysRevX.9.041061 (2019).
- 36 Guin, S. N. *et al.* Anomalous Nernst effect beyond the magnetization scaling relation in the ferromagnetic Heusler compound Co_2MnGa . *NPG Asia Materials* **11**, 16, doi:10.1038/s41427-019-0116-z (2019).
- 37 Ikhlas, M. *et al.* Large anomalous Nernst effect at room temperature in a chiral antiferromagnet. *Nature Physics* **13**, 1085-1090, doi:10.1038/nphys4181 (2017).
- 38 Wuttke, C. *et al.* Berry curvature unravelled by the anomalous Nernst effect in Mn_3Ge . *Physical Review B* **100**, 085111, doi:10.1103/PhysRevB.100.085111 (2019).
- 39 Liang, T. *et al.* Anomalous Nernst Effect in the Dirac Semimetal Cd_3As_2 . *Physical Review Letters* **118**, 136601, doi:10.1103/PhysRevLett.118.136601 (2017).